

# DASPy: A Python Toolbox for DAS Seismology

Minzhe Hu<sup>1</sup> and Zefeng Li<sup>1, 2\*</sup>

1. *Laboratory of Seismology and Physics of Earth's Interior, School of Earth and Space Sciences, University of Science and Technology of China, Hefei, China*

2. *Mengcheng National Geophysical Observatory, University of Science and Technology of China, Mengcheng, China*

Corresponding author: Zefeng Li ([zefengli@ustc.edu.cn](mailto:zefengli@ustc.edu.cn))

Manuscript submitted to *Seismological Research Letters*

June 20<sup>th</sup>, 2024

## **Abstract**

Distributed acoustic sensing (DAS) has emerged as a novel technology in geophysics, owing to its high sensing density, cost-effectiveness, and adaptability to extreme environments. Nonetheless, DAS differs from traditional seismic acquisition technologies in many aspects: big data volume, equidistant sensing, measurement of axial strain (strain rate), and noise characteristics. These differences make DAS data processing challenging for new hands. To lower the bar of DAS data processing, we develop an open-source Python toolbox called DASPy, which encompasses classic seismic data processing techniques, including preprocessing, filter, spectrum analysis, and visualization, and specialized algorithms for DAS applications, including denoising, waveform decomposition, channel attribute analysis, and strain-velocity conversion. Using openly available DAS data as examples, this paper makes an overview and tutorial on the eight modules in DASPy to illustrate the algorithms and practical applications. We anticipate DASPy to provide convenience for researchers unfamiliar with DAS data and help facilitate the rapid growth of DAS seismology.

## 1 Introduction

Distributed acoustic sensing (DAS) is an emerging vibration monitoring technology increasingly utilized in geophysics. It converts fiber optic cables into an ultradense seismic array with meter-scale spacing and a frequency range of 0.01 Hz to 100 kHz. DAS recovers axial strain or strain rate along the fiber-optic cable by measuring the subtle optical phase shift of backscattered light within the fiber (Lindsey & Martin, 2021; Zhan, 2019). Over recent years, it has been demonstrated useful in many seismological applications such as earthquake monitoring (Z. Li et al., 2021; Z. Li & Zhan, 2018; Lindsey et al., 2017; Nayak et al., 2021; Zeng et al., 2022), source property estimate (Chen, 2023; J. Li, Kim, et al., 2023; J. Li, Zhu, et al., 2023), subsurface imaging (Ajo-Franklin et al., 2019; Cheng et al., 2021; Dou et al., 2017; Luo et al., 2021; Nayak & Ajo-Franklin, 2021; Yang, Atterholt, et al., 2022), fault zone detection (Atterholt, Zhan, & Yang, 2022; Jousset et al., 2018; Lindsey et al., 2019; Yang, Zhan, et al., 2022) and urban seismology (Lindsey, Yuan, et al., 2020; X. Wang et al., 2021; T. Zhu et al., 2021). It has also been applied broadly outside seismology, such as volcanology (Jousset et al., 2022; Nishimura et al., 2021), oceanography (Lin et al., 2024; Sladen et al., 2019; Williams et al., 2019, 2022; Xiao et al., 2022), glaciology (Hudson et al., 2021; Walter et al., 2020), marine biology (Bouffaut et al., 2022; Landrø et al., 2022; Rørstadbotnen et al., 2023; Wilcock et al., 2023), and meteorology (Hong et al., 2024; T. Zhu & Stensrud, 2019).

DAS produces data gathers with regular spacing, similar to exploration seismic data. Hence, one may process DAS data with software for exploration data, such as Seismic Unix (Cohen & Stockwell, 2008) and Madagascar (<http://www.reproducibility.org>). However, compared to conventional seismic arrays in earthquake seismology, DAS differs in several key aspects, especially the voluminous data and uniaxial measurement of strain or strain rate (Z. Li, 2021; Lindsey & Martin, 2021; Zhan, 2019). The noise composition of DAS tends to be more complex due to its different self-noise, common-mode noise, and traffic noise for often along-road fibers (Bakku, 2015; Costa et al., 2019; Lindsey, Rademacher, et al., 2020; Zhirnov et al., 2019). These differences often require different processing techniques from those for conventional seismometers, making it challenging for researchers newly using DAS data.

Inspired by the success of ObsPy for conventional seismic data processing (Beyreuther et al., 2010), we believe that a new Python processing package specifically designed for DAS data could facilitate the development of DAS seismology. We notice that an ongoing project, called DASCORE, is developing a Python package for reading and writing, visualization, and basic processing of DAS data (Chambers et al., 2024). In this study, in addition to the functionalities offered by DASCORE, we aim to provide a wider diversity of practical data processing tools dedicated for DAS applications. This new open-source Python package is named DASP and comprises two primary components: a set of basic tools including modules for preprocessing, filtering,

frequency attributes and visualization, and another set of advanced tools including modules for channel analysis, waveform decomposition, denoising and strain-velocity conversion (Fig. 1). As follows, we showcase the key functionalities using various publicly available datasets (Fig. 2) and ensure that the experiments can be easily replicated by readers.

## 2 Basic Tools

### 2.1 Classic processing techniques

Typical seismic data processing includes filtering, frequency attribute analysis and certain preprocessing methods. We wrap these techniques for 2-dimensional DAS data, eliminating the need for iterating over channels. For example, the Python code below bandpass filters the data from the RAPID dataset (Wilcock & Ocean Observatories Initiative., 2023; <http://piweb.ooirsn.uw.edu/das/>; Figure 2a) between 15 and 27 Hz and yields a spectrogram averaged over 100 channels and a frequency-wavenumber (FK) spectrum (Figure 3). This dataset was collected offshore central Oregon and recorded various signals including fin whale calls, northeast Pacific blue whale A and B calls, and ship noises (Wilcock et al., 2023).

```
>>> from daspy.basic_tools.filter import bandpass
>>> from daspy.basic_tools.freqattributes import spectrogram, fk_transform
>>>
>>> data_filtered = bandpass(data, fs, 15, 27, detrend=True, taper=0.04)
>>> spec, f1, t = spectrogram(data[4880-50:4880+50], fs=fs, nperseg=256, noverlap=246,
                             nfft=1024, detrend=True)
>>> fk, f2, k = fk_transform(data, dx, fs)
```

92

## 93 2.2 Visualization

94 The function, `plot`, can be used to visualize 2-dimensional DAS data. It offers a  
95 number of optional parameters to accommodate the users' requirements for plotting a  
96 variety of data types, such as waveforms, spectra, spectrograms, and FK spectra. Below  
97 is the Python code for visualizing the data in the previous example: unfiltered and  
98 filtered data, the spectrogram and the FK spectrum (Figure 3). The bandpass filtered  
99 waveform reveals high-frequency fin whale calls, with amplitudes approximately four  
100 to five orders of magnitude lower than the ocean wave signals (Figure 3b). The  
101 spectrogram demonstrates the sequential production of high- and low-frequency calls  
102 by the fin whale (Figure 3c). The FK spectrum reveals an apparent velocity of this  
103 acoustic signal exceeding 1400 m/s along the axial direction of the optical cable (Figure  
104 3d).

105

```
>>> from daspy.basic_tools.visualization import plot
>>>
>>> fig, ax = plt.subplots(4, 1, figsize=(7,8))
>>> plot(data, dx=dx, fs=fs, ax=ax[0], transpose=True, x0=xmin*dx, xlabel=False,
        colorbar_label='Strain')
>>> plot(data_filtered, dx=dx, fs=fs, ax=ax[1], transpose=True, x0=xmin*dx,
        xlabel=False, colorbar_label='Strain')
>>> plot(Zxx, fs=fs, obj='spectrogram', ax=ax[2], f=f1, t=t, vmin=2e-8, vmax=3e-6,
        ylim=[0, 40])
>>> plot(fk, obj='fk', ax=ax[3], f=f2, k=k, xlim=[-0.025, 0.025], ylim=[0, 40],
        vmin=0.05, vmax=0.2)
>>> plt.tight_layout(pad=0.5)
>>> plt.savefig('figure3.pdf', dpi=800)
```

106

107

## 3 Advanced Tools

### 3.1 Channel analysis

DAS channels have equidistant spacing but the location of each channel is often unknown and requires tap tests. Besides, the linearity and ground coupling of the fibers often need to be taken care of. We develop three functions for channel location and quality analysis: channel location interpolation, turning point detection, and low-quality channel checking.

Channel location interpolation for DAS is calculated using two types of inputs: points with known channel numbers, and optional fiber spatial track points without channel numbers. Points with known channel numbers are typically acquired through tap tests and are often sparse. The spatial fiber track points are used to constrain the array geometry. They are optional but dense track points are particularly useful for accurate location interpolation. Fig. 2a shows examples of the two DAS arrays of the RAPID dataset (Wilcock & Ocean Observatories Initiative., 2023). In DASPy, we implemented the interpolation method used by the RAPID team, in which interpolation is performed after the coordinates are projected to the Universal Transverse Mercator (UTM) coordinate system.

The turning point detection function determines the points where the fiber strike varies noticeably based on the given channel coordinates or based on waveform coherency

across neighboring channels. The application of the coordinate-based detection function to Brady's geothermal field DAS array (University of Wisconsin, 2016a; <https://gdr.openet.org/submissions/829>; Fig. 2c) produces results consistent with those of Piana Agostinetti et al. (2022). As cross-channel waveform coherency is not only affected by the fiber strike angle, but also controlled by other factors including the quality of the backscattered light, coupling conditions and small-scale scatterers at different locations, its results could be less stable than those of coordinate-based computations assuming the coordinates are accurate. However, when the coordinates are unavailable or inaccurate, inference from cross-channel waveform coherency could be an alternative.

The channel quality checking function detects segments with obvious poor coupling (e.g., zip-tied loops of telecommunication cables) by identifying outliers of waveform energy along the fiber. It fits the waveform energy (the square of the amplitudes) variations with channels by a high-order polynomial and removes the fitted polynomial from the data. A threshold of four times of standard deviation below the median is set to identify the outliers. We assume that poor coupling tends to be spatially continuous. Hence, isolated normal values among a group of outliers would be identified as bad channels and vice versa. Using this function, we assess the channel quality of Ridgecrest DAS (Fig. 2d) with 15 seconds of traffic noise (Atterholt, 2021; <https://data.caltech.edu/records/1955>, Fig. 4). Our waveform-based detection results



are generally consistent with the hand-picked results of Atterholt, Zhan, Shen, et al. (2022) (Fig. 4b-f), except for the initial segment which was identified from a priori knowledge during field installation. It is noteworthy that the spikes (Fig. 4a) do not significantly influence the low-quality channel detection because we use a robust fit for the waveform energy (abnormal points are excluded from fitting).

### 3.2 Data denoising

As aforementioned, DAS data are often mixed with complex types of noise. DASPy integrates functions for the removal of typical noise types, including spike noise (Bakku, 2015), common-mode noise (Lindsey, Rademacher, et al., 2020), stochastic noise (Costa et al., 2019), and coherent noise. DASPy constructs a denoising module that incorporates three methods that take advantage of different noise properties.

Spikes are unusually large amplitudes (Fig. 5a) and could be caused by laser frequency drift or laser noise (Zhirnov et al., 2019). The spike removal function first applies the across-channel median filter and then the across-time median filter to generate a median map from the absolute amplitudes. Points with amplitudes exceeding a predefined threshold of the median map are identified as spikes. All spikes are subsequently substituted with interpolated values from adjacent channels. The spike removal function is validated using an earthquake waveform recorded by the Stanford-I DAS array (Fig. 2b and Fig. 5a-b; Biondi et al., 2017; Martin et al., 2017).

171

172 Common-mode noise, also known as in-phase noise is generated by vibrations of the  
173 optoelectronic system and arises on all channels simultaneously (Fig. 5d). DASP  
174 employs spatial averaging of waveforms to obtain common mode noise. Subsequently,  
175 we compute the correlation coefficient with the channel record and the common-mode  
176 noise, multiply the common-mode noise by the coefficient, and subtract it from the  
177 channel record. We evaluate the common-mode noise removal algorithm using a  
178 segment of offshore channels of the RAPID dataset (Wilcock & Ocean Observatories  
179 Initiative, 2023; Fig. 2a). The processing effectively mitigates the common-mode noise  
180 (Fig. 5d-e).

181

182 The inherent stochastic noise in DAS data is primarily caused by instrumental  
183 deficiencies such as sampling error and phase noise (Costa et al., 2019). The fast  
184 discrete curvelet transform (FDCT) (E. Candès et al., 2006; E. J. Candès & Donoho,  
185 2004) is used to obtain an effective non-adaptive sparse representation of the regular-  
186 spaced DAS seismic data and remove stochastic noise (Atterholt, Zhan, Shen, et al.,  
187 2022). The basis functions of curvelet transform are defined as polar wedges in the FK  
188 domain and represent the object position, scale, and angle. The curvelet denoising  
189 function uses a silent DAS recording to estimate stochastic noise. After FDCT, the  
190 amplitude of the curvelet coefficients is used as an empirical threshold. By default,  
191 DASP employs a soft threshold to remove stochastic noise in the curvelet domain. We

apply curvelet denoising to the spike-removed waveform of Stanford-1 DAS (Biondi et al., 2017; Martin et al., 2017; Fig. 2b and Fig. 5b), resulting in a notable reduction in stochastic noise before the arrival of P waves (Fig. 5c).

Coherent noise can be defined as any coherent signal that are not of interest. For example, for studies on an earthquake, a traffic signal is coherent noise; for studies on traffic footprints, an earthquake signal is coherent noise. Coherent noise can be removed by applying velocity screening in either the curvelet transform or the FK transform. In this case, coherent noise removal is treated as wavefield decomposition based on apparent velocity, which will be elaborated upon in the subsequent section.

### *3.3 Wavefield decomposition*

Image processing techniques, such as the 2D Fast Fourier Transform (e.g., FK transform in DAS data processing) and FDCT, have been widely used in the decomposition of 2D DAS wavefields, such as the separation of seismic signals and traffic noise and the separation of direct seismic waves and locally scattered seismic waves (Atterholt, Zhan, Shen, et al., 2022; Williams et al., 2022). DASPpy integrates the FK filtering and curvelet windowing techniques in the decomposition module.

Each point within the FK domain corresponds to a specific apparent velocity. In wavefield decomposition, the FK filter method employs a velocity threshold for

separation, followed by an inverse transform to produce low-speed and high-speed waveforms. Analogously, the curvelet basis utilized by the curvelet transform are wedges on the FK domain, with specific velocity ranges. The curvelet window technique separates the curvelet coefficients of the curvelet basis with different velocities. Therefore, the effects of these two techniques are nearly identical, which can be clearly determined in the FK domain of the separated waveforms. Both wavefield decomposition techniques are evaluated on stripping traffic noise from seismic waveform from the Ridgecrest DAS array (Z. Li et al., 2021; Fig. 2d). The results show that both techniques effectively enhance the signal-to-noise ratio without significant difference (Fig. 6).

### *3.4 Conversion to ground motions*

DAS measures strain or strain rate, in contrast to ground-motion velocity and displacement used in typical seismology studies. Strain and strain rate can be converted to particle velocity and acceleration by multiplying apparent phase velocity. The difficulty of such conversion lies in the accurate estimation of apparent phase velocity of every wiggle. DASP integrates three methodologies for converting strain/strain rate into ground-motion velocity: FK rescaling (Lindsey, Rademacher, et al., 2020), curvelet transform (Yang, Atterholt, et al., 2022), and time-domain slowness determination (Lior et al., 2021). The FK rescaling method is implemented by multiplying each point in the FK domain by its corresponding apparent velocity (slope in the FK domain). Similarly,

the basis functions of the curvelet transform, which are defined in the FK domain, also correspond to varying velocity ranges. The curvelet transform conversion method multiplies each curvelet coefficient by the median velocity of its basis function. The coefficients of the largest scale basis functions, which represents waves with all velocity ( $-\infty$  to  $+\infty$ ), is set to zero. The time-domain slowness determination method obtains the apparent velocity at each time step by searching for the maximal semblance.

These three methods are tested using an  $M_L$  4.3 earthquake recorded by a co-located DAS and seismometer array in the Brady Hot Springs (University of Wisconsin, 2016b; University of Wisconsin, 2016c; <https://gdr.openet.org/submissions/848>; <https://gdr.openet.org/submissions/846>; Fig. 3c), following H. F. Wang et al. (2018). We define a nodal geophone and a DAS channel whose distance is less than 5 m as a geophone-channel pair. Among 238 geophones and 8,621 DAS channels, we match a total of 344 geophone-channel pairs. For each geophone-channel pair, we find the corresponding linear DAS segment (Fig. 2c) and rotate the three-component geophone recording to the axial fiber direction. The original DAS strain rate recordings are integrated to strain in the time domain, and converted to velocity using FK rescaling, curvelet transform and time-domain slowness determination methods respectively (Fig. 7). We correct the DAS data timing (-1.048 s) using the GPS timing of nodal seismometers, and cross-correlate the waveforms of each geophone-channel pair with time shift less than  $\pm 0.01$  seconds. All waveforms are bandpass filtered to 1-5 Hz.

255

256 We evaluate the cross-correlation coefficient between the converted DAS velocity and  
257 the rotated geophone velocity. For all 344 geophone-channel pairs, 104, 71 and 0 pairs  
258 obtain cross-correlation coefficients greater than 0.7 after FK rescaling, curvelet  
259 transformation and time-domain slowness determination, respectively. For this  
260 particular case, the curvelet transform and the time-domain slowness determination  
261 have limitations. Most linear segments consist of about 100 channels, which is not quite  
262 enough for curvelet transform at larger scales. The largest scale curvelet coefficients,  
263 which are set to zero, miss more details, resulting in smaller amplitudes of the converted  
264 waveforms (Fig. 7). As for time-domain slowness determination methods, the  
265 assumption of monochromatic wavefields makes it difficult to recover the complex  
266 shallow surface scattered waves and earthquake coda waves.

267

## 268 **4 Discussion and Conclusions**

269 DASPpy aims to offer a user-friendly, integrated Python toolkit that facilitates the  
270 analysis and processing of DAS data. Overall, the toolkit includes "basic tools" of  
271 preprocessing, filtering, spectrum analysis, and visualization techniques and "advanced  
272 tools" of channel attribute analysis, noise removal, wavefield decomposition, and  
273 strain-velocity conversion.

274

DASPy can read and write a variety of DAS file formats, including .h5, .segv/.sgy, .tdms and .pkl (used for storing `daspy.Section` instances). These formats are often required by other open-source software. For example, PhaseNet-DAS (W. Zhu et al., 2023) take input in .h5 or .segv format. DASPy also supports reading DAS-RCN format as a `daspy.Section` instance which inherits the attributes from source DAS-RCN files (Lai et al., 2024). One may note that DASCORE supports more reading formats than DASPy. Also, ObsPy provides IO support for almost all traditional seismological formats, such as SAC and MiniSEED. Therefore, we provide methods (`Section.to_obs_py_stream`, `Section.to_dascore_patch`, `Section.from_obs_py_stream`, and `Section.from_dascore_patch`) for mutual transformation between `daspy.Section` instances and ObsPy's `Stream` instances (Beyreuther et al., 2010) and DASCORE's `Patch` instances (Chambers et al., 2024). These conversion functions allow smooth data flow between ObsPy, DASCORE and DASPy.

DASPy operates in the form of functions, which are designed to accommodate as many optional parameters as possible, and with sensible default values. All functions within DASPy are implemented as methods of the `daspy.Section` class. This approach is advantageous in that data attributes are stored within the class and avoid the need for manual entry. Calling functions and using methods of `daspy.Section` class are functionally equivalent, providing flexibility to suit users' needs.

296

297 Moreover, DASPy is currently programmed in pure Python for ease of use and  
298 modification but in some cases computational efficiency is compromised. Consequently,  
299 processing continuous data with a large number of channels and/or a high sampling rate  
300 could take a long time. As an example, downsampling a 30-second waveform recorded  
301 at 1000 Hz by a 10,000-channel DAS array takes 12.08 seconds. Therefore, we suggest  
302 that users consider implementing CPU parallelization when undertaking large tasks.  
303 Future development of DASPy could include exploring the potential of shared libraries  
304 to replace computationally intensive functions.

305

306 With aforementioned designs, DASPy can be easily incorporated into the data up- and  
307 down-stream tasks. The following is an example code snippet that combines DASPy  
308 and ObsPy (Beyreuther et al., 2010), for a typical task phase picking in earthquake  
309 monitoring:

```
>>> from daspy import read
>>> from obspy.signal.trigger import classic_sta_lta, trigger_onset
>>>
>>> sec = (
>>>     read('raw_data.h5')
>>>     .spike_removal()
>>>     .downsampling(xint=10, tint=10)
>>>     .fk_filter(fmin=1, fmax=15, vmin=2000)
>>> )
>>> sec.plot()
>>> sec.save('preprocessed_data.h5')
>>> onsets = []
>>> for d in sec.data:
>>>     cft = classic_sta_lta(d, nsta=int(0.5*sec.fs), nlta=int(5*sec.fs))
>>>     onsets.append(trigger_onset(cft, thres1=5, thres2=4))
```

310



The code reads in DAS data into an instance of `daspy.Section`, removes spike noise, performs a tenfold downsampling in both distance dimension (stacking every 10 channels into one) and time dimension (after an automatic lowpass filter), separates signal with frequency of 1-15Hz and apparent velocity less than 2000 m/s using FK filter. Subsequently, the preprocessed data is visualized, saved and fed into ObsPy to compute the short-term average/long-term average (STA/LTA; Allen & Rex, 1982) and to generate triggered picks.

As shown in the previous example, we envision that users can take advantage of DASPy to develop advanced packages developing new functions and/or modules (such as earthquake monitoring, ambient noise imaging, and traffic detection algorithms). We welcome users to contribute to the improvement and expansion of the DASPy project. Also, to foster a community of compatible packages, we add instructions for potential developers about how to contribute to the DASPy platform (<https://github.com/HMZ-03/DASPy/blob/main/CONTRIBUTING.md>). Developers are recommended to fork the DASPy repository on Github (<https://github.com/HMZ-03/DASPy/>) and submit their modifications and additions through pull requests.

## **Data and Resources**

The RAPID dataset is openly available at <http://piweb.ooirsn.uw.edu/das/>. The traffic signals recorded by the Ridgecrest DAS can be downloaded from

<https://data.caltech.edu/records/31emd-wmv98>. The Stanford DAS-1 dataset from PubDAS is accessible via the link [https://app.globus.org/file-manager?origin\\_id=706e304c-5def-11ec-9b5c-f9dfb1abb183&origin\\_path=%2F](https://app.globus.org/file-manager?origin_id=706e304c-5def-11ec-9b5c-f9dfb1abb183&origin_path=%2F). The earthquake waveforms recorded by Brady's Geothermal Field DAS and seismometer array are available at <https://gdr.openei.org/submissions/848> and <https://gdr.openei.org/submissions/846>. The DASPpy python package is open source and available at <https://github.com/HMZ-03/DASPpy/>. We include tutorials in both English and Chinese (<https://daspy-tutorial.readthedocs.io/en/latest/>, <https://daspy-tutorial-cn.readthedocs.io/zh-cn/latest/>) and a Jupyter notebook for quick use (<https://github.com/HMZ-03/DASPpy/blob/main/document/example.ipynb>). All websites were last accessed in June 2024.

## Acknowledgements

We appreciate the constructive comments from the Editor in Chief Allison Bent, the Associate Editor and two anonymous reviewers. We are grateful to Bin Luo for publishing code for reading multiple DAS data formats (<https://github.com/RobbinLuo/das-toolkit/blob/main/DasTools/DasPrep.py>) and to Zhongwen Zhan for the earthquake data from the Ridgecrest DAS array (Fig. 6). We thank Feng Cheng, Xiangfang Zeng and Jiaxuan Li for their helpful discussions on the project and Yanlan Hu and Jun Zhu for their support on coding. This research is

352 supported by the National Key R&D Program of China (No. 2022YFC3005602) and  
353 Anhui Provincial Key R&D Program (No. 2022m07020002).

354

#### 355 **Declaration of Competing Interests**

356 The authors acknowledge there are no conflicts of interest recorded.

357

## References

- Ajo-Franklin, J. B., Dou, S., Lindsey, N. J., Monga, I., Tracy, C., Robertson, M., et al. (2019). Distributed Acoustic Sensing Using Dark Fiber for Near-Surface Characterization and Broadband Seismic Event Detection. *Scientific Reports*, 9(1), 1–14. <https://doi.org/10.1038/s41598-018-36675-8>
- Allen, & Rex. (1982). Automatic Phase Pickers: Their Present Use and Future Prospects. *Bulletin of the Seismological Society of America*, (6), 225–242.
- Atterholt, J. (2021). Earthquake Waveforms from Curvelet-denoising Paper (Data Supplement) (1.0) [Data set]. CaltechDATA. <https://doi.org/10.22002/D1.1955>
- Atterholt, J., Zhan, Z., Shen, Z., & Li, Z. (2022). A unified wavefield-partitioning approach for distributed acoustic sensing. *Geophysical Journal International*, 228(2), 1410–1418. <https://doi.org/10.1093/gji/ggab407>
- Atterholt, J., Zhan, Z., & Yang, Y. (2022). Fault zone imaging with distributed acoustic sensing: body-to-surface wave scattering. *Journal of Geophysical Research: Solid Earth*, 127(6), 1–17. <https://doi.org/10.1029/2022jb024329>
- Bakku, S. K. (2015). Fracture Characterization from Seismic Measurements in a Borehole. *PhD Thesis*.
- Beyreuther, M., Barsch, R., Krischer, L., Megies, T., Behr, Y., & Wassermann, J. (2010). ObsPy: A python toolbox for seismology. *Seismological Research Letters*, 81(3), 530–533. <https://doi.org/10.1785/gssrl.81.3.530>

378 Biondi, B., Martin, E., Cole, S., Karrenbach, M., & Lindsey, N. (2017). Earthquakes  
 379 analysis using data recorded by the Stanford DAS array. In *SEG Technical*  
 380 *Program Expanded Abstracts 2017* (pp. 2752–2756).  
 381 <https://doi.org/10.1190/segam2017-17745041.1>

382 Bouffaut, L., Taweesintananon, K., Kriesell, H. J., Rørstadbotnen, R. A., Potter, J. R.,  
 383 Landrø, M., et al. (2022). Eavesdropping at the Speed of Light: Distributed  
 384 Acoustic Sensing of Baleen Whales in the Arctic. *Frontiers in Marine Science*,  
 385 9(July), 1–13. <https://doi.org/10.3389/fmars.2022.901348>

386 Brady’s Geothermal Field DAS and DTS Surface and Borehole Array Metadata [Data  
 387 set]. (2016). University of Wisconsin. <https://doi.org/10.15121/1261907>

388 Brady’s Geothermal Field DAS Earthquake Data [Data set]. (2016). University of  
 389 Wisconsin. <https://doi.org/10.15121/1334285>

390 Brady’s Geothermal Field Nodal Seismometer Earthquake Data [Data set]. (2016).  
 391 University of Wisconsin. <https://doi.org/10.15121/1334284>

392 Candès, E., Demanet, L., Donoho, D., & Ying, L. (2006). Fast discrete curvelet  
 393 transforms. *Multiscale Modeling and Simulation*, 5(3), 861–899.  
 394 <https://doi.org/10.1137/05064182X>

395 Candès, E. J., & Donoho, D. L. (2004). New tight frames of curvelets and optimal  
 396 representations of objects with piecewise C2 singularities. *Communications on*  
 397 *Pure and Applied Mathematics*, 57(2), 0219–0266.  
 398 <https://doi.org/10.1002/cpa.10116>

399 Chambers, D., Jin, G., Tourei, A., Hafiz Saeed Issah, A., Lellouch, A., Martin, E. R.,  
400 et al. (2024). DASCORE: a Python Library for Distributed Fiber Optic Sensing.

401 Chen, X. (2023). Source parameter analysis using distributed acoustic sensing – an  
402 example with the PoroTomo array. *Geophysical Journal International*, 2207–  
403 2213.

404 Cheng, F., Chi, B., Lindsey, N. J., Dawe, T. C., & Ajo-Franklin, J. B. (2021).  
405 Utilizing distributed acoustic sensing and ocean bottom fiber optic cables for  
406 submarine structural characterization. *Scientific Reports*, 11(1), 1–14.  
407 <https://doi.org/10.1038/s41598-021-84845-y>

408 Cohen, J. K., & Stockwell, J. W. (2008). CWP/SU: Seismic Un\*x: an open source  
409 software package for seismic research and processing. *Center for Wave*  
410 *Phenomena, Colorado School of Mines*, 40.

411 Costa, L., Martins, H. F., Martín-López, S., Fernández-Ruiz, M. R., & González-  
412 Herráez, M. (2019). Fully Distributed Optical Fiber Strain Sensor With 10–12  
413  $\epsilon/\sqrt{\text{Hz}}$  Sensitivity. *Journal of Lightwave Technology*, 37(18), 4487–4495.  
414 <https://doi.org/10.1109/JLT.2019.2904560>

415 Dou, S., Lindsey, N., Wagner, A. M., Daley, T. M., Freifeld, B., Robertson, M., et al.  
416 (2017). Distributed Acoustic Sensing for Seismic Monitoring of the Near  
417 Surface: A Traffic-Noise Interferometry Case Study. *Scientific Reports*, 7(1), 1–  
418 12. <https://doi.org/10.1038/s41598-017-11986-4>

419 Hong, H., Wang, B., Lu, G., Li, X., Ge, Q., Xie, A., et al. (2024). Tracking Lightning  
 420 Through 3D Thunder Source Location With Distributed Acoustic Sensing.  
 421 *Journal of Geophysical Research: Atmospheres*, 129(4), 1–13.  
 422 <https://doi.org/10.1029/2023JD038882>  
 423 Hudson, T. S., Baird, A. F., Kendall, J. M., Kufner, S. K., Brisbourne, A. M., Smith,  
 424 A. M., et al. (2021). Distributed Acoustic Sensing (DAS) for Natural  
 425 Microseismicity Studies: A Case Study From Antarctica. *Journal of Geophysical*  
 426 *Research: Solid Earth*, 126(7), 1–19. <https://doi.org/10.1029/2020JB021493>  
 427 Jousset, P., Currenti, G., Schwarz, B., Chalari, A., Tilmann, F., Reinsch, T., et al.  
 428 (2018). Dynamic strain determination using fibre-optic cables allows imaging of  
 429 seismological and structural features. *Nature Communications*, 13(1).  
 430 <https://doi.org/10.1038/s41467-022-29184-w>  
 431 Jousset, P., Currenti, G., Schwarz, B., Chalari, A., Tilmann, F., Zuccarello, L., et al.  
 432 (2022). Fibre optic distributed acoustic sensing of volcanic events. *Nature*  
 433 *Communications*. <https://doi.org/10.1038/s41467-022-29184-w>  
 434 Lai, V. H., Hodgkinson, K. M., Porritt, R. W., & Mellors, R. (2024). Toward a  
 435 Metadata Standard for Distributed Acoustic Sensing (DAS) Data Collection.  
 436 *Seismological Research Letters*, 95(3), 1986–1999.  
 437 <https://doi.org/10.1785/0220230325>  
 438 Landrø, M., Bouffaut, L., Kriesell, H. J., Potter, J. R., Rørstadbotnen, R. A.,  
 439 Taweessintananon, K., et al. (2022). Sensing whales, storms, ships and

440 earthquakes using an Arctic fibre optic cable. *Scientific Reports*, 12(1), 1–10.

441 <https://doi.org/10.1038/s41598-022-23606-x>

442 Li, J., Zhu, W., Biondi, E., & Zhan, Z. (2023). Earthquake focal mechanisms with

443 distributed acoustic sensing. *Nature Communications*, 14(1), 4181.

444 <https://doi.org/10.1038/s41467-023-39639-3>

445 Li, J., Kim, T., Lapusta, N., Biondi, E., & Zhan, Z. (2023). The break of earthquake

446 asperities imaged by distributed acoustic sensing. *Nature*, 620(October 2022).

447 <https://doi.org/10.1038/s41586-023-06227-w>

448 Li, Z. (2021). Recent advances in earthquake monitoring i: Ongoing revolution of

449 seismic instrumentation. *Earthquake Science*, 34(2), 177–188.

450 <https://doi.org/10.29382/eqs-2021-0011>

451 Li, Z., & Zhan, Z. (2018). Pushing the limit of earthquake detection with distributed

452 acoustic sensing and template matching: A case study at the Brady geothermal

453 field. *Geophysical Journal International*, 215(3), 1583–1593.

454 <https://doi.org/10.1093/gji/ggy359>

455 Li, Z., Shen, Z., Yang, Y., Williams, E., Wang, X., & Zhan, Z. (2021). Rapid

456 Response to the 2019 Ridgecrest Earthquake With Distributed Acoustic Sensing.

457 *AGU Advances*, 2(2). <https://doi.org/10.1029/2021av000395>

458 Lin, J., Fang, S., He, R., Tang, Q., Qu, F., Wang, B., & Xu, W. (2024). Monitoring

459 ocean currents during the passage of Typhoon Muifa using optical-fiber



distributed acoustic sensing. *Nature Communications*, 15(1).  
<https://doi.org/10.1038/s41467-024-45412-x>

Lindsey, N. J., & Martin, E. R. (2021). Fiber-Optic Seismology. *Annual Review of Earth and Planetary Sciences*, 309–338.

Lindsey, N. J., Craig Dawe, T., & Ajo-Franklin, J. B. (2019). Illuminating seafloor faults and ocean dynamics with dark fiber distributed acoustic sensing. *Science*, 366(6469), 1103–1107. <https://doi.org/10.1126/science.aay5881>

Lindsey, N. J., Yuan, S., Lellouch, A., Gualtieri, L., Lecocq, T., & Biondi, B. (2020). City-Scale Dark Fiber DAS Measurements of Infrastructure Use During the COVID-19 Pandemic. *Geophysical Research Letters*, 47(16), 1–8.  
<https://doi.org/10.1029/2020GL089931>

Lindsey, N. J., Rademacher, H., & Ajo-Franklin, J. B. (2020). On the Broadband Instrument Response of Fiber-Optic DAS Arrays. *Journal of Geophysical Research: Solid Earth*, 125(2), 1–16. <https://doi.org/10.1029/2019JB018145>

Lior, I., Sladen, A., Mercerat, D., Ampuero, J. P., Rivet, D., & Sambolian, S. (2021). Strain to ground motion conversion of distributed acoustic sensing data for earthquake magnitude and stress drop determination. *Solid Earth*, 12(6), 1421–1442. <https://doi.org/10.5194/se-12-1421-2021>

Luo, B., Trainor-Guitton, W., Bozdag, E., LaFlame, L., Cole, S., & Karrenbach, M. (2021). Horizontally orthogonal distributed acoustic sensing array for earthquake- And ambient-noise-based multichannel analysis of surface waves.

481 *Geophysical Journal International*, 222(3), 2147–2161.

482 <https://doi.org/10.1093/GJI/GGAA293>

483 Martin, E., Castillo, C., Cole, S., Sawasdee, P., Yuan, S., Clapp, R., et al. (2017).

484 Seismic monitoring leveraging existing telecom infrastructure at the SDASA:

485 Active, passive, and ambient-noise analysis. *The Leading Edge*, 36, 1025–1031.

486 <https://doi.org/10.1190/tle36121025.1>

487 Nayak, A., & Ajo-Franklin, J. (2021). Measurement of surface-wave phase-velocity

488 dispersion on mixed inertial seismometer – distributed acoustic sensing seismic

489 noise cross-correlations. *Bulletin of the Seismological Society of America*,

490 111(6), 3432–3450. <https://doi.org/10.1785/0120210028>

491 Nayak, A., Ajo-Franklin, J., & Team, the I. V. D. F. (2021). Distributed Acoustic

492 Sensing Using Dark Fiber for Array Detection of Regional Earthquakes.

493 *Seismological Research Letters*, 92(4), 2441–2452.

494 <https://doi.org/10.1785/0220200416>

495 Nishimura, T., Emoto, K., Nakahara, H., Miura, S., Yamamoto, M., Sugimura, S., et

496 al. (2021). Source location of volcanic earthquakes and subsurface

497 characterization using fiber-optic cable and distributed acoustic sensing system.

498 *Scientific Reports*, 11(1), 1–12. <https://doi.org/10.1038/s41598-021-85621-8>

499 Piana Agostinetti, N., Villa, A., & Saccorotti, G. (2022). Distributed acoustic sensing

500 as a tool for subsurface mapping and seismic event monitoring: A proof of

501 concept. *Solid Earth*, 13(2), 449–468. <https://doi.org/10.5194/se-13-449-2022>

502 Rørstadbotnen, R. A., Eidsvik, J., Bouffaut, L., Landrø, M., Potter, J.,  
 503 Taweessintananon, K., et al. (2023). Simultaneous tracking of multiple whales  
 504 using two fiber-optic cables in the Arctic. *Frontiers in Marine Science*,  
 505 10(April), 1–15. <https://doi.org/10.3389/fmars.2023.1130898>  
 506 Sladen, A., Rivet, D., Ampuero, J. P., De Barros, L., Hello, Y., Calbris, G., &  
 507 Lamare, P. (2019). Distributed sensing of earthquakes and ocean-solid Earth  
 508 interactions on seafloor telecom cables. *Nature Communications*, 10(1), 1–8.  
 509 <https://doi.org/10.1038/s41467-019-13793-z>  
 510 Walter, F., Gräff, D., Lindner, F., Paitz, P., Köpfli, M., Chmiel, M., & Fichtner, A.  
 511 (2020). Distributed acoustic sensing of microseismic sources and wave  
 512 propagation in glaciated terrain. *Nature Communications*, 11(1).  
 513 <https://doi.org/10.1038/s41467-020-15824-6>  
 514 Wang, H. F., Zeng, X., Miller, D. E., Fratta, D., Feigl, K. L., Thurber, C. H., &  
 515 Mellors, R. J. (2018). Ground motion response to an ML 4.3 earthquake using  
 516 co-located distributed acoustic sensing and seismometer arrays. *Geophysical*  
 517 *Journal International*, 213(3), 2020–2036. <https://doi.org/10.1093/GJI/GGY102>  
 518 Wang, X., Zhan, Z., Williams, E. F., Herráez, M. G., Martins, H. F., & Karrenbach,  
 519 M. (2021). Ground vibrations recorded by fiber-optic cables reveal traffic  
 520 response to COVID-19 lockdown measures in Pasadena, California.  
 521 *Communications Earth & Environment*, 2(1), 1–9.  
 522 <https://doi.org/10.1038/s43247-021-00234-3>

523 Wilcock, W. S. D., & Ocean Observatories Initiative. (2023). Rapid: A Community  
 524 Test of Distributed Acoustic Sensing on the Ocean Observatories Initiative  
 525 Regional Cabled Array [Data set]. Ocean Observatories Initiative.  
 526 <https://doi.org/doi.org/10.58046/5J60-FJ89>  
 527 Wilcock, W. S. D., Abadi, S., & Lipovsky, B. P. (2023). Distributed acoustic sensing  
 528 recordings of low-frequency whale calls and ship noise offshore Central Oregon.  
 529 *JASA Express Letters*, 3(2), 026002. <https://doi.org/10.1121/10.0017104>  
 530 Williams, E. F., Fernández-Ruiz, M. R., Magalhaes, R., Vanthillo, R., Zhan, Z.,  
 531 González-Herráez, M., & Martins, H. F. (2019). Distributed sensing of  
 532 microseisms and teleseisms with submarine dark fibers. *Nature Communications*,  
 533 10(1), 1–11. <https://doi.org/10.1038/s41467-019-13262-7>  
 534 Williams, E. F., Zhan, Z., Martins, H. F., Fernández-Ruiz, M. R., Martín-López, S.,  
 535 González-Herráez, M., & Callies, J. (2022). Surface Gravity Wave  
 536 Interferometry and Ocean Current Monitoring With Ocean-Bottom DAS.  
 537 *Journal of Geophysical Research: Oceans*, 127(5), 1–27.  
 538 <https://doi.org/10.1029/2021JC018375>  
 539 Xiao, H., Gaite, B., & Ruiz-barajas, S. (2022). Locating the precise sources of high-  
 540 frequency microseisms using distributed acoustic sensing. *Geophysical Research*  
 541 *Letters*, 0–31. <https://doi.org/10.1029/2022GL099292>  
 542 Yang, Y., Zhan, Z., Shen, Z., & Atterholt, J. (2022). Fault Zone Imaging With  
 543 Distributed Acoustic Sensing: Surface-To-Surface Wave Scattering. *Journal of*

544 *Geophysical Research: Solid Earth*, 127(6).

545 <https://doi.org/10.1029/2022jb024329>

546 Yang, Y., Atterholt, J. W., Shen, Z., Muir, J. B., Williams, E. F., & Zhan, Z. (2022).

547 Sub-Kilometer Correlation Between Near-Surface Structure and Ground Motion

548 Measured With Distributed Acoustic Sensing. *Geophysical Research Letters*,

549 49(1). <https://doi.org/10.1029/2021GL096503>

550 Zeng, X., Bao, F., Thurber, C. H., Lin, R., Wang, S., Song, Z., & Han, L. (2022).

551 Turning a Telecom Fiber-Optic Cable into an Ultradense Seismic Array for

552 Rapid Postearthquake Response in an Urban Area. *Seismological Research*

553 *Letters*, 93(2 A), 853–865. <https://doi.org/10.1785/0220210183>

554 Zhan, Z. (2019). Distributed acoustic sensing turns fiber-optic cables into sensitive

555 seismic antennas. *Seismological Research Letters*, 91(1), 1–15.

556 <https://doi.org/10.1785/0220190112>

557 Zhirnov, A., Stepanov, K., Chernutsky, A., Fedorov, A., Nesterov, E., Svelto, C., et

558 al. (2019). Influence of laser frequency drift in phase-sensitive optical time-

559 domain reflectometry. *Optics and Spectroscopy*, 127.

560 <https://doi.org/10.1134/S0030400X1910031X>

561 Zhu, T., & Stensrud, D. J. (2019). Characterizing Thunder-Induced Ground Motions

562 Using Fiber-Optic Distributed Acoustic Sensing Array. *Journal of Geophysical*

563 *Research: Atmospheres*, 124(23), 12810–12823.

564 <https://doi.org/10.1029/2019JD031453>

565 Zhu, T., Shen, J., & Martin, E. R. (2021). Sensing Earth and environment dynamics  
 566 by telecommunication fiber-optic sensors: An urban experiment in Pennsylvania,  
 567 USA. *Solid Earth*, 12(1), 219–235. <https://doi.org/10.5194/se-12-219-2021>  
 568 Zhu, W., Biondi, E., Li, J., Yin, J., Ross, Z. E., & Zhan, Z. (2023). Seismic Arrival-  
 569 time Picking on Distributed Acoustic Sensing Data using Semi-supervised  
 570 Learning. *Nature Communications*, 14(1), 1–17. [https://doi.org/10.1038/s41467-](https://doi.org/10.1038/s41467-023-43355-3)  
 571 023-43355-3

572 **Full mailing address for each author**

573 Minzhe Hu: Laboratory of Seismology and Physics of Earth's Interior, School of Earth  
 574 and Space Sciences, University of Science and Technology of China, No.96, JinZhai  
 575 Road Baohe District, Hefei, Anhui, 230026, P.R.China.

576 Zefeng Li: Laboratory of Seismology and Physics of Earth's Interior, School of Earth  
 577 and Space Sciences, University of Science and Technology of China, No.96, JinZhai  
 578 Road Baohe District, Hefei, Anhui, 230026, P.R.China.

579

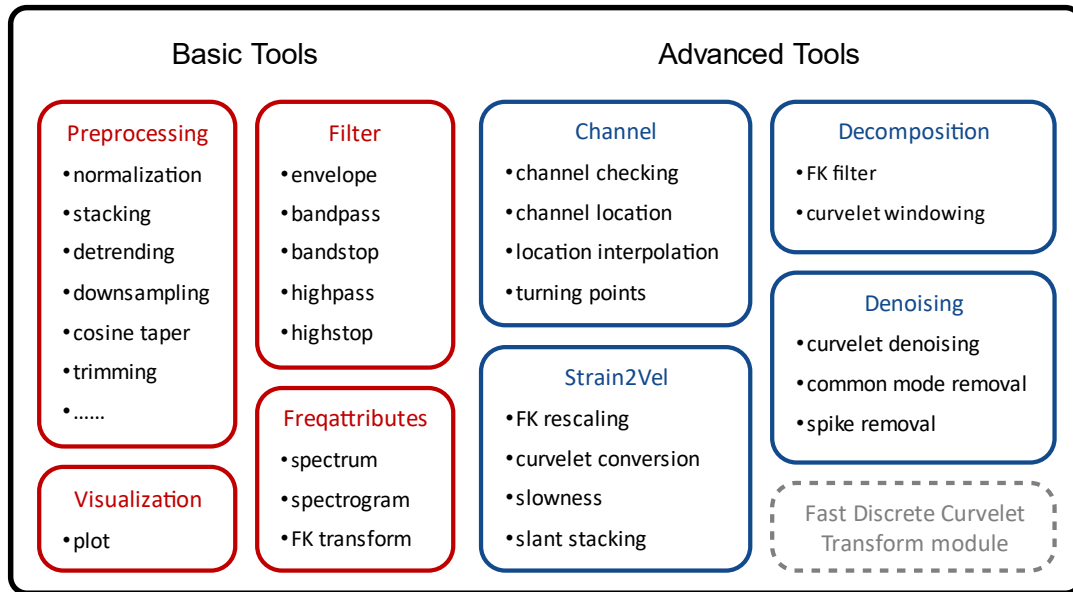


**Figure 1.** Main structure of DASPpy toolbox. Each block indicates a module composed of multiple user-facing functions. The modules for basic tools are shown in red boxes, and modules for advanced tools are shown in blue boxes. The module within the gray dotted box is specifically built for discrete fast curvelet transforms.

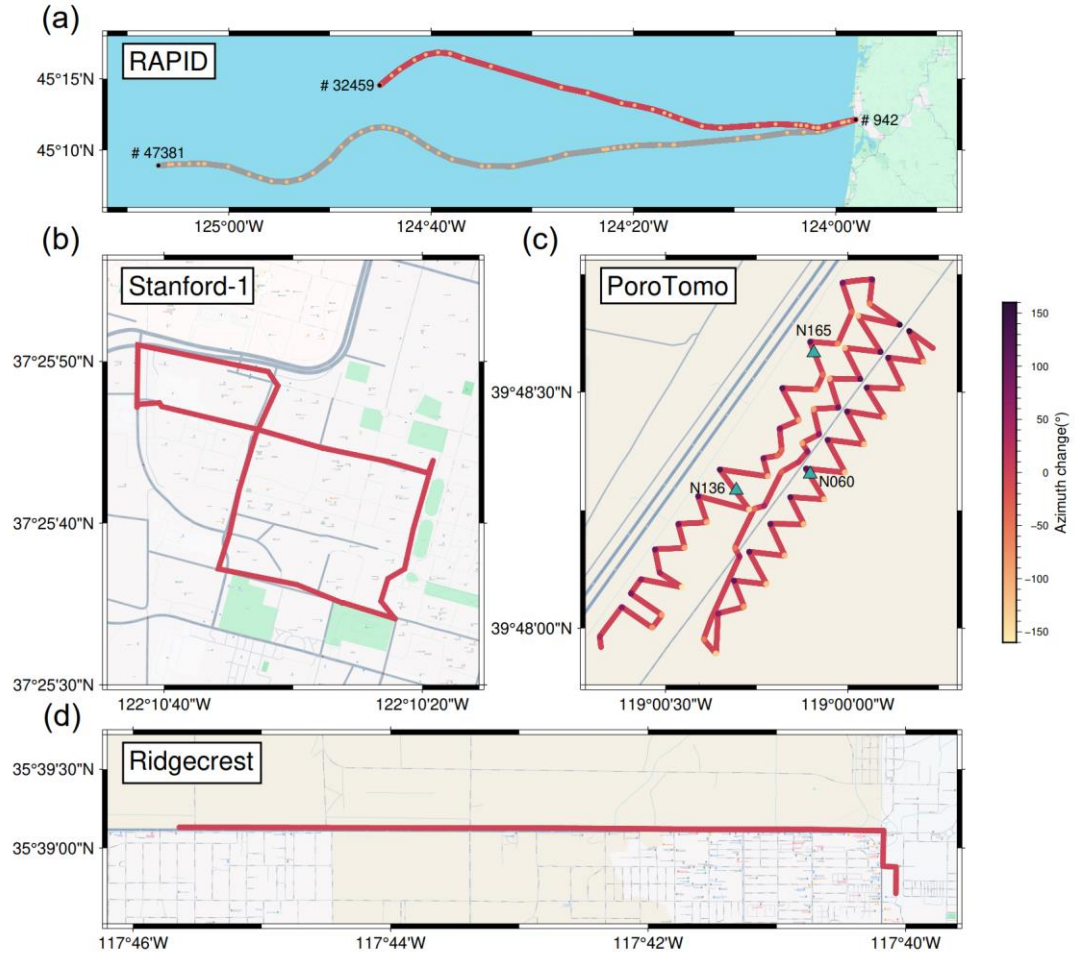


**Figure 2.** Geometry of DAS arrays whose data we used for testing. (a) RAPID DAS arrays that land at Pacific City, Oregon (Wilcock & Ocean Observatories Initiative., 2023). The red line indicates the array that we utilized for our test (referring to the north cable here), which is the same for (b) and (d). The grey line indicates the south cable, whose data are not used. The black dots represent three points along the cable with known coordinates and channel numbers, while the orange dots represent the those with known coordinates but unknown channel number. (b) Stanford campus array in California (Biondi et al., 2017; Martin et al., 2017). (c) Brady's geothermal field DAS array (University of Wisconsin, 2016b) and three co-located geophone stations



596 (University of Wisconsin, 2016c) in Nevada. The color of the DAS cable indicates the  
597 azimuth change of the cable before and after the corresponding channel. (d) DAS arrays  
598 started after the 2019  $M_w$ 7.1 Ridgecrest earthquake, California (Atterholt, Zhan, Shen,  
599 et al., 2022; Z. Li et al., 2021).  
600

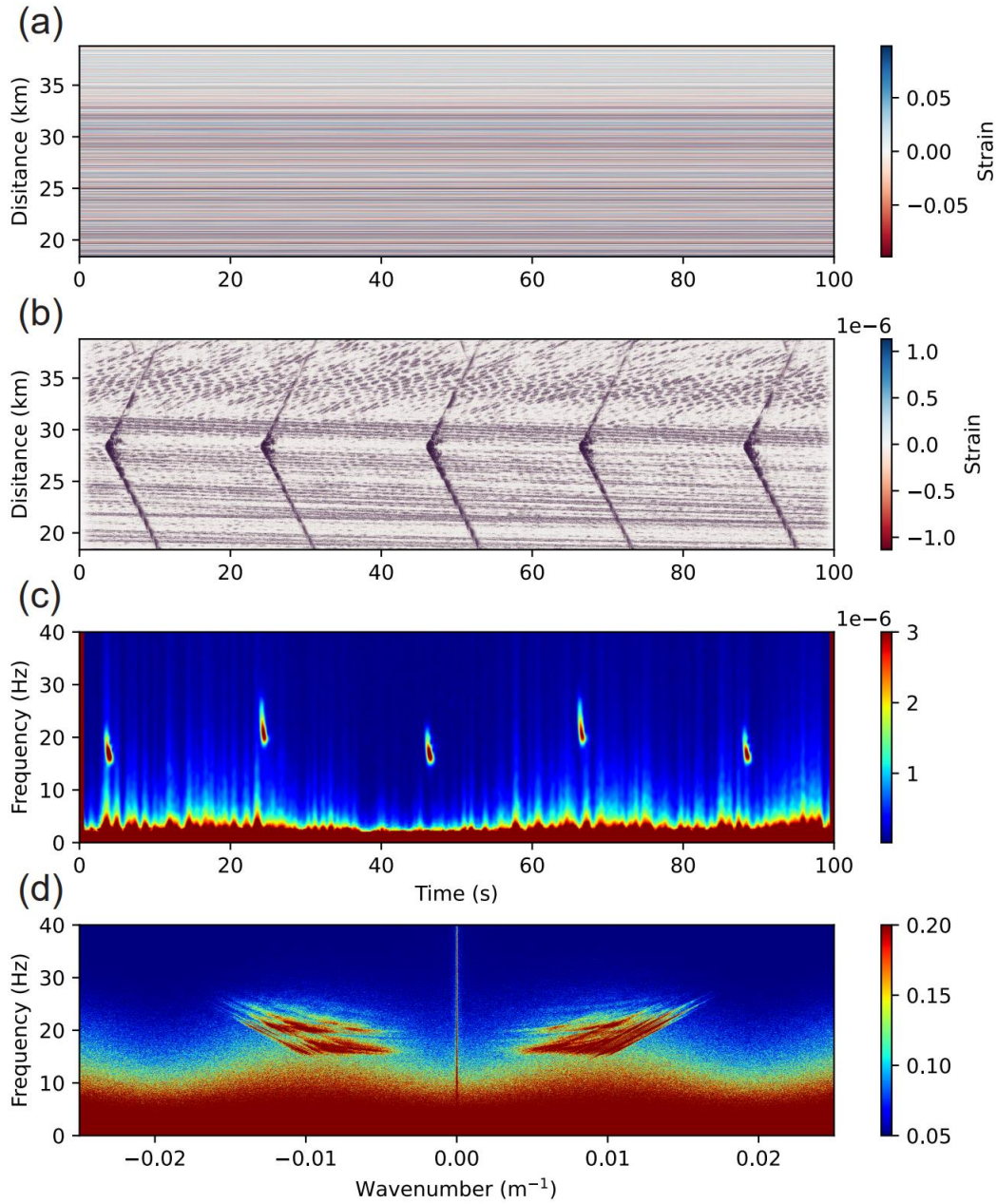


**Figure 3.** Demonstration of signal processing and visualization. (a) Original strain recording for 100 seconds beginning on November 4, 2021, 01:59:02 UT, recorded by the Optasense interrogator channel 9000-19000 on north ocean-bottom cable from RAPID dataset (Wilcock & Ocean Observatories Initiative., 2023). (b) Filter to 15-27 Hz, following Wilcock et al. (2023). (c) Spectrogram averaged over 100 channels. (d) FK spectrum calculated from 2D fast Fourier transform.

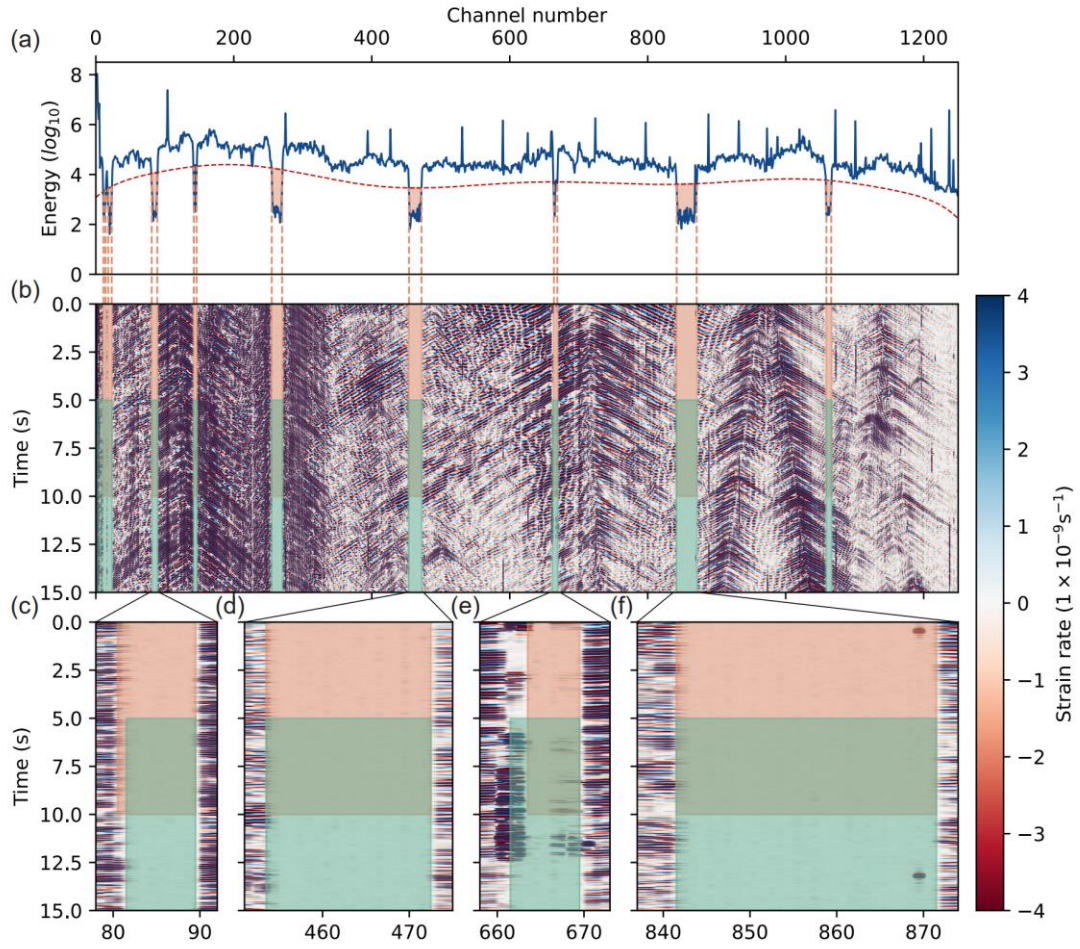


**Figure 4.** Bad channel detection of the DAS array near Ridgecrest, CA. (a) Energy curve (blue line) and thresholds (red dotted line) for bad channel detection. (b) DAS recording of 15-second traffic noise (Atterholt, 2021) used for bad channel detection. Orange areas indicate bad channels detected by our function, while green areas are bad channels picked by Atterholt, Zhan, Shen, et al. (2022). (c)-(f) Zoom-in plot of four parts of the DAS recording. Channel 81 (c) and channels 662&663 (e) are identified differently by our function and Atterholt, Zhan, Shen, et al. (2022).



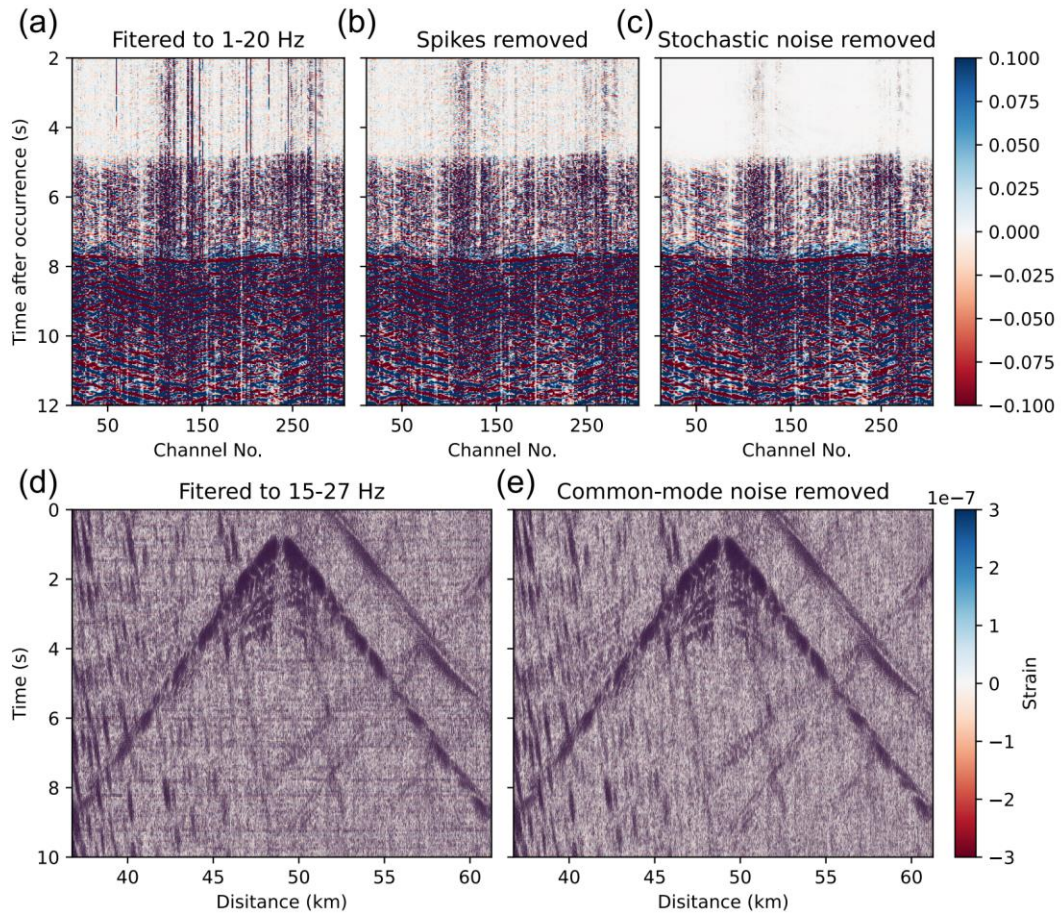


**Figure 5.** Cases of wavefield denoising. (a) Waveforms of an  $M_D$  2.8 earthquake (<https://earthquake.usgs.gov/earthquakes/eventpage/nc73940346/executive>) recorded by Stanford-1 DAS array (Biondi et al., 2017; Martin et al., 2017). Bad channels are removed and bandpass filter to 1-20 Hz. (b) Waveforms with spikes removed based on (a). (c) Waveforms with stochastic noise removed by curvelet transform based on (b). (d) Strain recording filtered to 15 to 27 Hz for 10 seconds beginning on November 4, 2021, 01:59:22 UT, recorded by the Optasense interrogator on north ocean-bottom cable from RAPID dataset (Wilcock & Ocean Observatories Initiative., 2023). (e) Waveforms with common-mode noise removed based on (d).

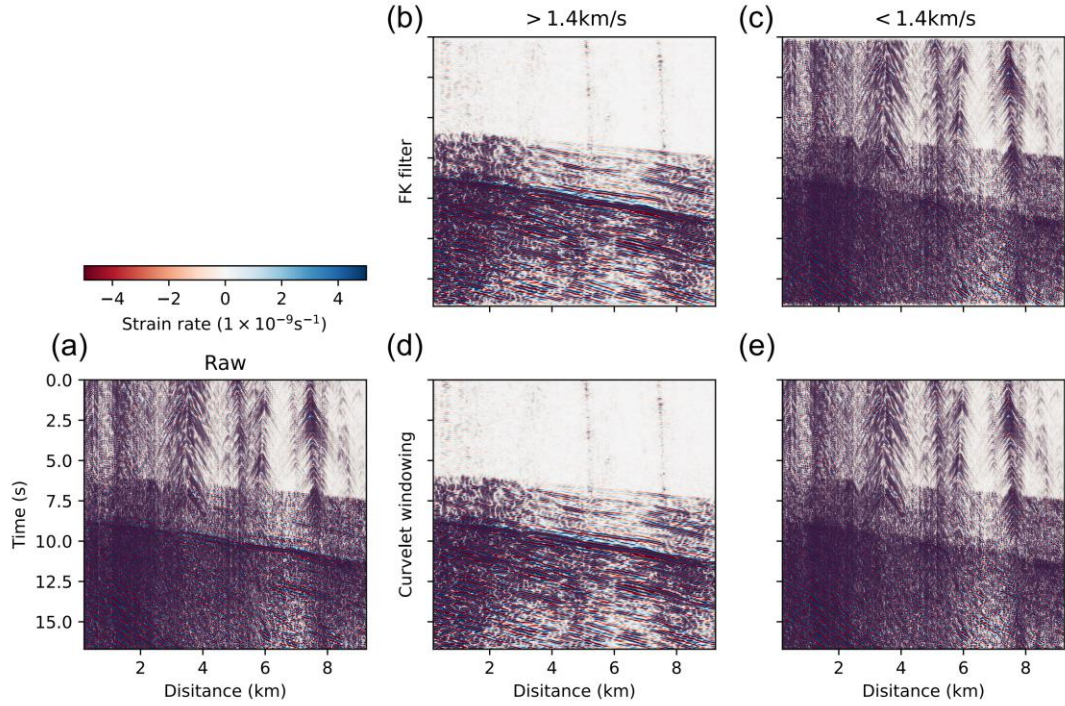


**Figure 6.** An example of wavefield decomposition. (a) Waveforms of an  $M_L$  2.6 earthquake (<https://earthquake.usgs.gov/earthquakes/eventpage/ci38972328/executive>) recorded by Ridgecrest DAS array (Z. Li et al., 2021), with spikes removed. (b) Waveforms with an FK filter to retain energy with an apparent velocity  $> 1.4 \text{ km/s}$  (cosine tapered from 1.2–1.6 km/s). (c) Waveforms with an FK filter to retain energy with an apparent velocity  $< 1.4 \text{ km/s}$  (cosine tapered from 1.2–1.6 km/s). (d) Waveforms with curvelet windowing to retain energy with an apparent velocity  $> 1.4 \text{ km/s}$ . (e) Waveforms with curvelet windowing to retain energy with an apparent velocity  $< 1.4 \text{ km/s}$ .

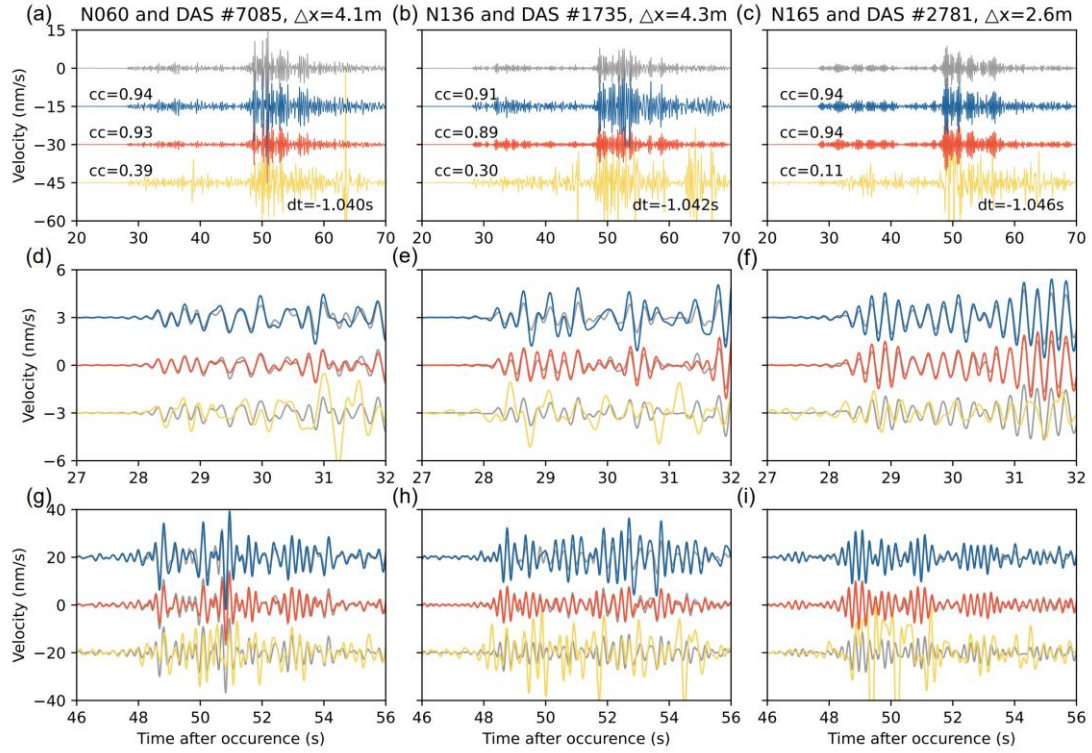


**Figure 7.** Conversion from strain to velocity by three methods of  $M_L$  4.3 Hawthorne earthquake (<https://earthquake.usgs.gov/earthquakes/eventpage/nn00536374>) recorded by Brady's geothermal field DAS array. (a)-(c) Rotated geophone velocity (grey), and velocity converted from integrated DAS strain by FK-rescaling (blue), curvelet transform (red) and time-domain slowness determination (yellow), same as below. All waveforms are bandpass filtered to 1-5 Hz. (d)-(f) Zoom-in window for P arrival of (a)-(c). (g)-(i) Zoom-in window for S arrival of (a)-(c).